

# EFFECT OF ARGON GAS ON FLUID FLOW IN A CONTINUOUS SLAB CASTING MOLD

B. G. Thomas and X. Huang

Department of Mechanical and Industrial Engineering  
University of Illinois at Urbana-Champaign  
1206 West Green Street  
Urbana, IL 61801

## ABSTRACT

To help understand the complex effects of multiphase fluid flow, superheat dissipation and grade intermixing during the continuous casting of steel slabs, three-dimensional mathematical models have been developed and applied to predict multiphase fluid flow and its associated heat and mass transfer in this process. The effects of gas bubble injection into the liquid are simulated using a continuum model, which calculates the volume fraction and velocities of the gas, and its effect on the liquid flow. Turbulence has been incorporated using the standard K- $\epsilon$  turbulence model, without any modification due to the presence of either the gas bubbles or inclusions. Reasonable agreement has been achieved between predicted velocities and the corresponding measurements and observations in full-scale water models, both with and without gas injection.

The effects of argon gas bubble injection on the flow related phenomena are investigated with simulations of a typical steel slab caster. Argon bubbles alter the flow pattern in the upper recirculation zone in proportion with increasing gas fraction and decreasing bubble size, shifting the impingement point and recirculation zones upward. Argon injection also causes superheat to be removed higher in the caster, moves the hot spot upwards, lowers the peak heat flux, and increases heat extraction from the wide face and meniscus regions. During a steel grade transition, argon injection slightly affects slab surface composition, but has no effect on intermixing in the slab interior.

## I. INTRODUCTION

Argon gas is employed at several stages in the continuous casting process (ladle, tundish, and mold) to encourage mixing, to help prevent nozzle clogging, and to promote the flotation of solid inclusion particles from the liquid steel. It enters the continuous casting mold after injection into the submerged entry nozzle (SEN), and eventually escapes from the liquid steel surface through the mold flux powder layer.

The injected argon gas bubbles influence the flow pattern, which has corresponding effects on superheat extraction, grade mixing, and inclusion movement. The extent of this effect is intensified by the volume expansion of the gas bubbles in the high-temperature molten steel, which

could increase its ambient-temperature volume up to 5 times, under typical casting conditions. Therefore, even a small rate of argon gas injection, (3% volume flow ratio of gas to liquid steel at the SEN inlet), could result in up to 15% gas volume fraction in the mold, with significant effects on the flow pattern. The calculation of volume expansion of argon gas at typical casting conditions is given in Appendix I.

Experimental measurements on an operating continuous casting machine are very difficult, dangerous, and expensive. Multiphase flow phenomena, particularly volumetric expansion of the gas, are also difficult to simulate using physical water models. On the other hand, the recent development of numerical modeling provides an efficient tool for understanding and solving this kind of problem in material processing. Several mathematical models have been applied to argon-steel flow and its associated heat and mass transfer in gas-agitated vessels, such as casting ladles.<sup>[1-5]</sup> Research efforts have also been dedicated to gas-liquid flow dynamics at room temperature, both experimentally with physical water models and numerically with mathematical models.<sup>[6-13]</sup>

Little work has been reported on two-phase flow in the continuous casting mold, especially at high temperature. One of the few studies, by Bessho et al.<sup>[14]</sup> compared the calculated flow pattern, gas holdup (volume fraction) and inclusion distribution in a full-scale water model with experimental measurements and observations. Although only one case was reported, the results showed that gas created a great change in the flow pattern.

The present work describes the development of three-dimensional (3-D) finite-difference models of two-phase flow of liquid steel with argon gas bubbles and its associated heat and mass transfer in the continuous slab casting mold. After verification with water models, the models are applied to investigate the effects of bubble size and injection rate on the flow pattern, superheat extraction and intermixing during a steel grade transition. In later work, the model will be extended to simulate the movement of inclusion particles.

The transient nature of flow in the mold, which causes problems such as surface turbulence, are known to be very important to steel quality. However, as a first step towards understanding this behavior, this work assumes a steady-state flow pattern and investigates the influence of argon gas injection on this flow pattern and related phenomena.

## II. GAS-LIQUID FLOW MODEL

Mathematical models have been developed to simulate 3-D gas-liquid two-phase flows, using the computational domain and grid of 60 x 34 x 16 nodes shown in Figure 1. Two-fold symmetry is assumed so only one quarter of the mold is modeled. The liquid velocities,  $v_x$ ,  $v_y$ ,  $v_z$ , and pressure,  $p$ , are calculated by solving the 3-D, incompressible, steady-state, mass and momentum conservation equations for a Newtonian fluid. The buoyancy force acting on the liquid due to the existence of gas bubbles was taken into account by adding an extra force term,  $f_g$ , into the liquid momentum equation in the vertical direction,  $z$ :

$$f_g = \alpha_g g \quad [1]$$



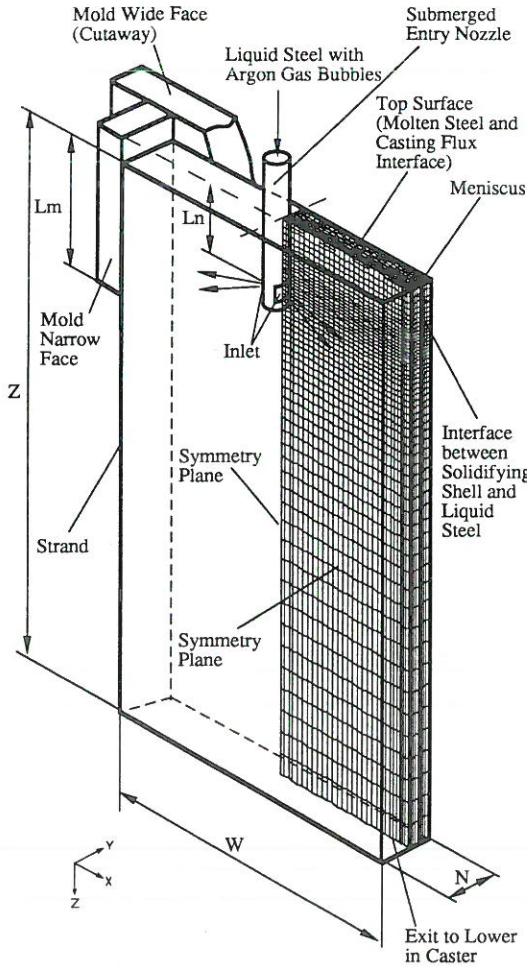


FIG. 1. Simulation domain and typical mesh used in 3D steel-argon two-phase flow model.

The Reynolds number in the caster, based on the hydraulic diameter, always exceeds 10,000 even far below the mold. This indicates that the flow is highly turbulent everywhere. Thus, the K- $\epsilon$  turbulence model is used in calculating velocities of the liquid phase.

Bubble dispersion in the gas-liquid mixture due to turbulent transport is calculated by solving a continuum conservation / diffusion equation similar to that used to model transport of a solute element, with the turbulent Schmidt Number,  $Sc_t$ , set to 1.

To simplify the problem, no momentum equation is solved for the gas phase. Instead, the bubbles are assumed to reach their steady-state terminal velocity in the vertical direction relative to the liquid phase,  $v_{gt}$ , immediately upon entering the domain. The gas bubbles are assumed to be spheres with a uniform size, whose terminal velocity is found according to an empirical correlation<sup>[15]</sup> that depends on bubble size:

$$v_{gt} = \exp(a_0) \exp(a_1 \ln d_g) \exp[a_2 (\ln d_g)^2] \quad [2]$$

$$a_0 = -8.373, a_1 = -2.6306, a_2 = -0.2500$$

## A. Boundary Conditions

### 1. Liquid Phase

Inlet boundary conditions, including jet angle, velocity profile, turbulent kinetic energy and its dissipation rate, are specified according to output from a separate three-dimensional finite element model of the nozzle, described elsewhere.<sup>[16-18]</sup> The inlet, shown in Figure 1, represents the plane between the nozzle port and the mold cavity. To simplify its geometry in the present mold model, a rectangular inlet area is adopted for both rectangle and circular nozzle ports.

Because fluid always flows out through the bottom portion of the nozzle outlet port and there is a small inward flow near the top portion<sup>[16-18]</sup>, the submergence depth used in the mold simulation refers to the distance from the top surface of the mold to the top of jet, which is at the top of the inlet. This explains the greater jet submergence depths,  $L_n$ , employed to simulate the corresponding experiments,  $L_o$ . The distance between the top surface and the position of the maximum out-flow from the nozzle is chosen to be the same in the simulation and the experiments.

For the outlet of the computational domain, which is a horizontal plane across the steel caster, and holes in the bottom of a physical water model, the normal gradients ( $\partial/\partial n$ ) of all variables, including  $v_x$ ,  $v_y$ ,  $v_z$ ,  $K$ ,  $\epsilon$ , and  $p$  are set to zero. The same boundary conditions are used for each node on a symmetry centerplane, except that the velocity component normal to the symmetry plane is set to zero. The top surface is treated the same as a symmetry plane and the small variations in the liquid level due to motion of the free surface are neglected.

The bottom of the physical water model domain is simplified to make it symmetrical. The bottom of the standard water model, Case A1 in Table I, was modeled with four holes in the symmetric half of the domain instead of four holes on just one side, as used in the experiments. This simplification is reasonable because it should have just a tiny effect on the flow only near the outlet holes and flow asymmetry was not observed in the physical water model.

Empirical "wall law" functions<sup>[19]</sup> are employed to define the tangential velocities,  $K$ , and  $\epsilon$  at the near-wall grid nodes in order to account for the steep gradients that exist near the walls. When simulating real steel casters, the domain extends up to, but not including, the mushy zone to avoid the computational difficulties associated with modeling latent heat evolution at the solidification front. The boundaries of the mesh along the narrow and wide face walls correspond to the dendrite tips forming the outer limit of the mushy zone. These boundaries are treated as very rough solid walls by reducing the roughness factor in the wall laws from 8.8 to 0.8.<sup>[18]</sup>

### 2. Gas Phase

A zero-gradient condition of gas bubble volume fraction,  $\sigma_g$ , is set for all boundaries except the inlet of the domain. This condition is consistent with no gas flow through the walls, while it allows gas to leave from the top surface, at the imposed relative terminal velocity. Gas could

also be carried from the bottom of the domain, if the terminal velocity did not greatly exceed the casting speed. At the inlet plane to the mold from the nozzle,  $\sigma_g$  is set to a constant,  $\sigma_{g0}$ , found according to Appendix II. This calculation accounts for the volume expansion of the gas bubbles due to the high temperature of the liquid steel and the pressure increase due to the height change.

#### B. Solution method

Owing to the simple rectangular geometry of the mold, a computer code based on finite difference calculations, MUPFAHT<sup>[20]</sup> has been chosen for this complex problem. The steady-state (elliptic) system of differential equations and boundary conditions is discretized into finite difference equations using a staggered grid and seven-point stencil of control volumes. To aid convergence, an upwinding scheme is employed for the advection terms in domains with high cell Reynolds number.<sup>[21]</sup> In addition, the source terms are linearized to increase diagonal dominance of the coefficient matrix.<sup>[21]</sup> The equations are solved with the Semi-Implicit Method of Pressure-Linked Equations algorithm, whose Alternating-Direction-semi-Implicit iteration scheme consists of 3 successive Tri-Diagonal-Matrix-Algorithm solutions (one for each coordinate direction) followed by a pressure-velocity-modification to satisfy the mass conservation equation.<sup>[21]</sup>

Obtaining reasonably-converged velocity and turbulence fields for this problem is difficult, owing to the high degree of recirculation. The current strategy employed is successive iteration using an under-relaxation factor of 0.2 or 0.3 until the maximum relative residual error and maximum relative error between successive solutions falls below 0.1 pct. Over 2500 iterations are required to achieve this, starting from an initial guess of zero velocity, which takes about 20 CPU hours on a Silicon Graphics 4D/35 workstation.

### III. HEAT TRANSFER MODEL FOR SUPERHEAT DISSIPATION

The dissipation of the superheat has an important influence on growth of the shell during the critical initial stages of solidification. It also has an important effect on surface defect formation and steel internal quality related to the microstructure. To investigate superheat dissipation in the continuous slab casting mold, a heat transfer model has been developed to compute temperature distribution within the liquid pool, heat transfer to the inside of the solidifying shell, and its effect on growth of the shell. This model solves a 3-D energy conservation equation, with greatly enhanced conductive heat transfer due to turbulent eddy motion.<sup>[19]</sup> The turbulent Prandtl number,  $Pr_t$  is set to the standard value of 0.9.<sup>[17, 22]</sup>

#### A. Boundary Conditions

Temperature across the inlet plane is simply fixed to the casting temperature,  $T_0$ . This temperature corresponds to a tundish temperature, because the temperature drop through the nozzle is very small.<sup>[23]</sup> Adiabatic conditions or zero normal temperature gradient conditions ( $\partial T/\partial n$ ) are used at the outlet plane and the symmetry centerplanes. For the top surface, calculations were made to estimate heat conduction through the molten flux and powder layers and

radiating to ambient.<sup>[18]</sup> To account for this heat loss, an equivalent thermal convection boundary condition is applied to the top surface, using the heat transfer coefficient,  $h$ , and ambient temperature,  $T_\infty$ .

To correspond with the flow boundary conditions, described in the last section, the boundaries of the computational domain for heat transfer are again assumed to be the dendrite tips, so the domain does not include the solidified shell and the mushy zone. A fixed temperature, nominally equal to the liquidus,  $T_{liq}$ , is imposed along these boundaries. The reduction of the domain due to the solidification is neglected because the solidifying shell is very thin in the mold region.

An empirical "thermal wall law"<sup>[19]</sup> is used to determine temperature at the near-wall grid nodes. Use of this thermal wall function was important to achieve an accurate heat balance. It is needed to calculate the heat flux due to superheat dissipation,  $q_{sh}$ , which in turn influences the growth of the solidifying steel shell.

This approach differs from other recent models, which couple the fluid flow and solidification calculations. The latter models use a function (based on flow through porous media) to radically reduce velocity and turbulence levels within the mushy zone.<sup>[24]</sup> By separating the fluid flow and solidification calculations, the present approach reduces the complexity needed in subsequent models of heat conduction and solidification of the shell. Results from the present model have been incorporated into a thermal stress and shrinkage model that includes coupled heat flow across the mold/shell gap.<sup>[25]</sup>

#### B. Effect of Argon Gas Bubbles

Argon gas bubbles may affect heat transfer in the caster in two ways: by affecting heat convection through their effect on flow velocities, and by enhancing turbulent heat conduction through increasing turbulence intensity. Only the former effect is incorporated into the present model. It is believed that the change of turbulence parameters due to gas bubbles has only a minor influence on the time-averaged flow pattern.<sup>[11]</sup> Based on this, gas bubbles may not have a significant effect on the time-averaged temperature distribution either.

#### C. Solution Methodology

The differential equations, together with the boundary conditions described above, were solved with the same finite difference schemes used for the flow models. Because heat transfer has negligible effect on the fluid flow, (i.e. there is only one-way coupling between the fluid flow and heat transfer models), previously converged solutions of the velocity and turbulence fields are input and kept unchanged during the solution of the temperature. Thus, only 30 minutes CPU time is needed on the SGI 4D/35 workstation.

### IV. MASS-TRANSFER MODEL FOR GRADE TRANSITION

A 3-D transient mass transfer model, consisting of three submodels, has been developed to calculate intermixing in both the strand and the solidified slab during a transition in steel grade<sup>[26]</sup>. The results presented here correspond to a "flying tundish change", where steel grade is changed



simultaneously with the ladle and tundish. The influence of argon gas bubble injection on mass transfer is automatically introduced through its effect on the time-averaged velocities, as done with heat transfer.

#### A. 3-D Transient Mass Transfer Model of Upper Strand

The first submodel calculates 3-D transient turbulent solute diffusion in the upper 6 m strand. This model calculates dimensionless composition, or "relative concentration" defined as:

$$C \equiv \frac{F(x, y, z, t) - F_{old}}{F_{new} - F_{old}} \quad [3]$$

where  $F(x, y, z, t)$  is the mass fraction of a given element at a specified position in the strand or slab;  $F_{old}$  and  $F_{new}$  are the specified fractions of that element in the pure old and new grades respectively.

The initial composition of element B is set to zero throughout the domain. A sudden transition from  $C=0$  to  $C=1$  was imposed at the inlet to start the simulation ( $z=0$  in the slab). Zero-gradient or "no mass diffusion" boundary conditions were given to the composition at the outlet plane, the symmetry planes and the top surface, as well as the wide and narrow walls. Thus, solute can only leave the domain by fluid transport across the outlet plane.

#### B. 1-D Mass Transfer Model of Lower Strand

Composition evolution must be calculated over the entire liquid pool of the strand (usually 20-40 m to the metallurgical length) before it is possible to predict the complete composition distribution in the final slabs. Fortunately, the initial 3-D results for the top 6 m show that the velocity profile in the lower region of the strand is quite uniform and close to that of turbulent flow through a duct. Thus, for economy, a 1-D mass transfer model was developed as the second submodel, to simulate the remaining domain beyond 6 m.

#### C. Slab Composition Model

Composition distribution in the final slab develops as the solidifying shell grows in thickness down the caster. The third submodel calculates the composition distribution in the final slab based on the 3-D time-varying concentration history of the strand, generated by the first two submodels. Composition at each point in the strand is assumed to evolve according to the calculated history until that point solidifies. The required distance down the strand for solidification is found using an assumed parabolic rate of shell growth:

$$\text{shell thickness} = k_{\text{shell}} * \sqrt{z/V_c} \quad [4]$$

TABLE I. SIMULATION CONDITIONS FOR FLOW MODEL

	Case A1 (51 mm by 76 mm Rectangular Port, Armco)	Case A2 <sup>†</sup> (51 mm by 89 mm Rectangular Port, Armco)	Case A3 <sup>†</sup> (51 mm Circular Port, Armco)	Case B1 (Long Model, Inland)	Case B2 <sup>††</sup> (Short Model, Inland)	Case C (Steel Caster)
$L_w$ (mm)	51			60		60
$L_h$ (mm)	66	46	36	38		38
$\alpha_o$ (°)	15 down		25 down	15 down		15 down
$\alpha$ (°)	25 down			25 down		24 down
$L_n$ (m)	0.1828		0.1778	0.265		0.265
$L_o$ (m)	0.1524			0.235		0.235
$Z$ (m)	2.152			3	1.12	3
$W$ (m)	1.93			1.32		1.32
$N$ (m)	0.229			0.22		0.22
$V_c$ (m/s)	0.0152			0.0167		0.0167
$E$	8.8			8.8		0.8
$\mu_o$ (Ns/m <sup>2</sup> )	0.001			0.001		0.0055
$\rho$ (kg/m <sup>3</sup> )	1000			1000		7020
$v_{x0}$ (m/s)	1.048	1.513	1.908	1.062		1.062
$v_{z0}$ (m/s)	0.489	0.672	0.848	0.427		0.471
$K_0$ (m <sup>2</sup> /s <sup>2</sup> )	0.0502	0.0281	0.0702	0.054		0.0502
$\epsilon_0$ (m <sup>2</sup> /s <sup>3</sup> )	0.457	0.705	1.335	0.447		0.457
Gas	Helium	None	None	None	Air	Argon
$Q_g$ (m <sup>3</sup> /s)	0, 0.00024	0	0	0	0.00034	0, 0.00011, 0.00024
$\sigma_{g0}$ (%)	0, 3%	0	0	0	5 %	0, 11%, 22%
$d_g$ (mm)	1, 5	None	None	None	1	1, 3, 5

<sup>†</sup> Unlisted values are the same as case A1.

<sup>††</sup> Unlisted values are the same as case B1.



#### D. Solution Method

Like the solution procedure for the heat transfer model, both the 3-D and 1-D transient diffusion equations are solved based on the velocities and turbulence properties from the flow model. The solution is obtained using a backward Eulerian method with variable time steps. A simulation of 960 seconds of casting requires about 50 time steps and 8 hours of CPU time on the SGI 4D/35 workstation.

#### V. TYPICAL MODEL FLOW RESULTS

The 3-D numerical model of two-phase flow, described in section II, can simulate flow in either the actual steel-slab continuous-casting machine, or in a physical water model of the process, by simple changes in the domain outlet boundary conditions, the liquid properties, and other simulation conditions. This section presents typical predictions of the flow pattern in a 2.15 m water model, which are similar in many respects to flow in the steel caster. After verification of the numerical model through comparisons with observations and measurements in the physical water model, it is then used to predict fluid flow and related behavior in a typical steel caster. The post processor FIPOST, of the commercial finite element program FIDAP,<sup>[27]</sup> was used to visualize and plot the results.

##### A. Typical Flow predictions in Water Model without Gas Injection

Figure 2 illustrates the three dimensional flow pattern predicted in the water model with no gas injection for typical conditions, Case A1 in Table I. For clarity of presentation, a velocity vector is drawn only at every eighth node in the grid. Figure 2 (a) views the centerplane section parallel to the wide face wall. The fluid leaves the nozzle as a strong jet, impinges upon the narrow face, then splits vertically to create upper and lower recirculation regions. Figure 2 (b) reveals the interior velocity vectors in transverse sections taken at 5 locations down the mold. Because the bifurcated nozzle sends flow into a relatively thin mold cavity, the resulting velocities are relatively uniform through the thickness of the mold over most of the mold interior. Down the corner near the impingement point, a weak vortex is formed, as the jet spreads across the narrow face and meets the incoming flow just off the corner along the wide face surface. Velocity components through the mold thickness are quite small everywhere except very near the outlet holes. Thus, flow in the mold can be characterized by the angle of the jet traversing the mold, the location of its impingement point on the narrow face, and by the location in the x-z plane of the centers of the recirculation zones: the "lower eye" and "upper eye". These flow parameters are illustrated in Figure 3.

##### B. Typical Flow Predictions in Water Model with Gas Injection

The influence of gas bubbles on the flow pattern is seen in Figures 3 (b) and 4 for simulation conditions Case A1 with a gas bubble size,  $d_g$ , of 1 mm hydraulic diameter and a gas volume fraction at the inlet plane to the mold cavity,  $\sigma_{g0}$ , of 3%. The buoyancy of the gas bubbles changes the flow pattern significantly in the upper region of the mold, even for this small amount of gas injection. When the bubbles are small, as assumed here, they travel with the jet and induce it to bend upwards to impinge at a slightly higher location on the narrow face wall. This upward

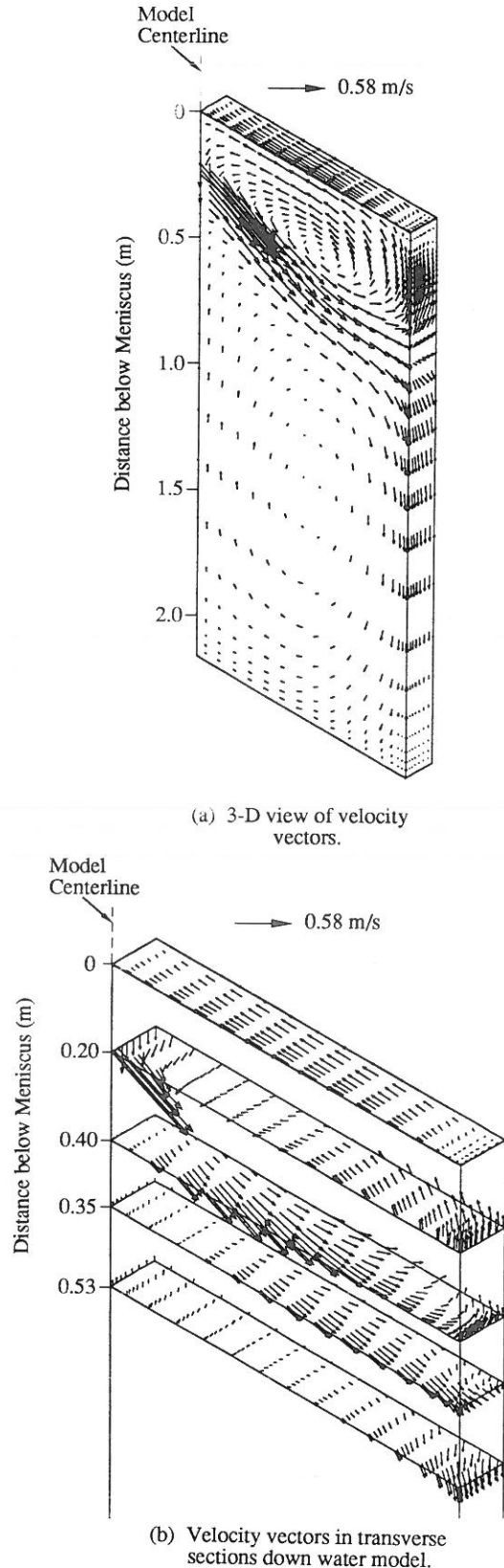


FIG. 2. Predicted flow patterns in water model (Case A1 in Table I without gas).

motion due to the bubbles is predicted to shift the location of the upper eye greatly toward the mold center and slightly upward to just above the nozzle port.

As the bubble-rich liquid in the central portion of the jet rises vertically, velocity gradients are created through the mold thickness. This effect is seen most clearly by comparing the 0.20 m slices in Figures 2(b) and 4. A horizontal recirculation region is predicted in the central region, and there is no unique location of the upper eye (Figure 4). As the rising bubble-rich liquid reaches the top surface, it slows down the flow of liquid across the top surface back toward the nozzle and creates a slight drift towards the wide faces. Both of these effects disrupt the mainly 2-D flow pattern found without gas.

Gas bubbles are predicted to have much less effect on the flow pattern in the lower portion of the mold. Compared to the flow pattern without gas, the lower recirculation zone appears very similar, with the lower eye raised only a small distance. The reason for this diminished effect is explained in Figure 5, which shows the predicted gas volume fraction in the water model under the same conditions as Figures 3(b) and 4. Due to the strong buoyancy force, which is proportional to the density difference between liquid and gas, most of the gas bubbles float upward to escape from the top surface during the time that the liquid jet travels from the nozzle port to the narrow face wall. Less than 5% of the bubbles even reach the vicinity of the narrow wall and even fewer enter the lower recirculation zone of the liquid flow. Thus, flow in the lower recirculation zone should be relatively unaffected by gas bubble injection.

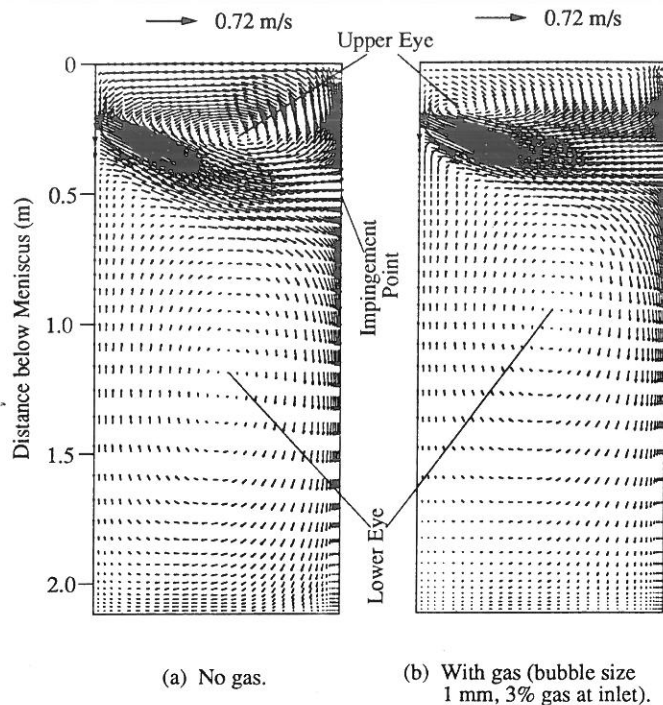


FIG. 3. Two-dimensional view of predicted flow patterns in water model (Case A1 in Table I).

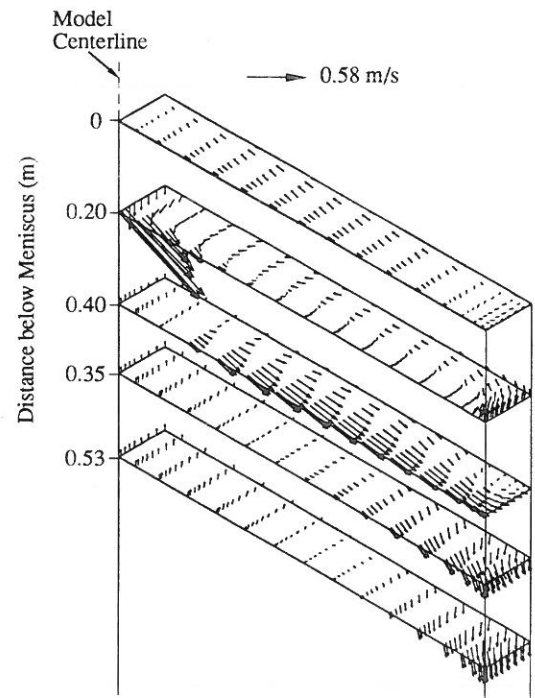


FIG. 4. Velocity vectors in transverse sections down water model (Case A1 in Table I, bubble size 1 mm, 3% gas at inlet).

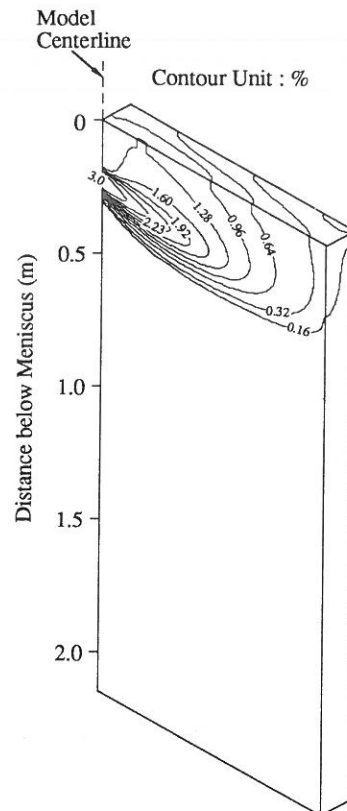


FIG. 5. Predicted gas volume fraction in water model (Case A1 in Table I, bubble size 1 mm, 3% gas at inlet).



## VI. PHYSICAL WATER MODEL EXPERIMENTS

To verify the flow model predictions, measurements of velocity profiles and flow pattern observations have been made with full-scale water models at Armco Research Center, Middletown, OH and Inland Steel, East Chicago, IN. The 1.93-m (76-in.) wide and 0.229-m (9-in.) thick "water caster", shown schematically in Figure 6, is a clear plastic representation of an actual slab caster used in the Armco Middletown Works, with its length shortened to 2.15 m. This physical model has 4 pipes located at the bottom of the wide face to allow removal of water at a volume flow rate corresponding to the casting speed.

The flow patterns were visualized in three ways: (1) blue ink injected as a pulse from the tundish slide gate; (2) observation of a flag constructed with thin film attached to a wooden dowel; (3) helium gas bubbles injected through the SEN. Observations using these three visualization methods were combined to estimate the average downward angle of the jet traversing the mold, the impingement point of the jet against the narrow face, and the locations of the centers of the upper and lower recirculation zones.

A hot-wire anemometer probe with a single-wire sensor was used to measure the velocity profiles. Carefully-measured resistance heating is provided to the wire to

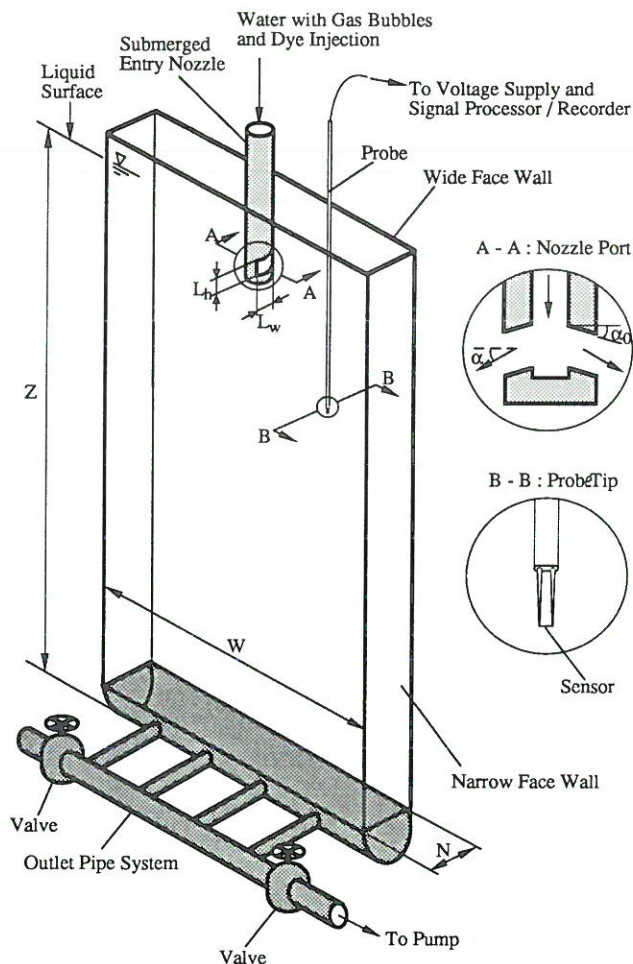


FIG. 6. Schematic of physical water model and hot wire anemometry apparatus for speed measurements.

balance the heat loss, which increases in proportion to the flow velocity component perpendicular to the wire. By orienting the sensor wire perpendicular to the wide-face wall, this probe was used to measure the speed component in the wide-face plane. The calibrated voltage signals from the sensor were recorded by both a strip chart and a needle, whose movements were dampened electronically to produce a partially time-averaged signal.

Measurements were taken at 50 mm intervals down various vertical lines from the top surface at the symmetry plane through the narrow face of the water model. Extra data points were measured near the nozzle port and impingement point, as determined by flow pattern visualization, because large velocity gradients were expected to exist in these regions. The probe was traversed manually after careful calibration of the system, including an adjustment for water temperature. A typical signal output from the strip chart recorder is shown in Figure 7. For this example, the time-averaged speed is 0.23 m/s and the standard deviation, containing 68% of the signals, is about 0.08 m/s. Note that the maximum range of the signal is  $\pm 0.18$  m/s, indicating the tremendous effect of the time-dependent turbulent fluctuations of the flow field. The jet is observed to "wander" around with time, producing a low-frequency variation in the velocity signal of 2 - 5 seconds. To account for this effect and to ensure that a true time-mean speed measurement was obtained, over two minutes of signal measurements were averaged to obtain each speed data point.

## VII. NUMERICAL MODEL VALIDATION

To validate the accuracy of the numerical flow model, described in section II, simulations were run to match the flow conditions in the full-scale physical water model, described in section VI. This section compares the numerical predictions with the experimental observations of flow pattern, gas bubble distribution, and speed measurements.

### A. Comparison with Flow Pattern Observations

The overall flow pattern calculated numerically is very similar to the flow pattern observed in the physical models. Table II quantitatively compares the flow parameters for simulation conditions, Case A1 in Table I, matching experiments performed at Armco Research.<sup>[28]</sup>

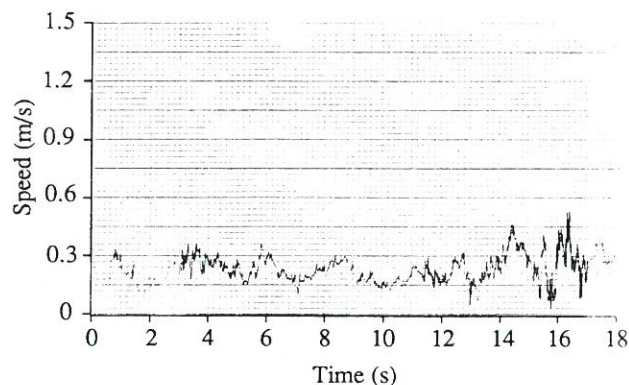


FIG. 7. Typical signal output from the strip chart record (mean velocity = 0.23 m/s; standard deviation = 0.08 m/s).

For the comparisons with gas, the gas volume fraction,  $\sigma_{g0}$ , of 3%, was chosen to match the flow rate of 0.00024 m<sup>3</sup>/s (30 standard cubic feet per hour) of helium injected into the physical model nozzle through a small tube. The bubble size of 5 mm was estimated both by visual observations and by examining photographs of the bubbles in the water model.

The five measurements of eye and impingement point location agree with the numerical predictions both with and without gas. The largest discrepancy is with the depth of the lower eye below the top liquid surface. The numerical model calculates a deeper lower eye than the experiments. This might occur because the jet in the physical model achieves fully-developed turbulent channel flow more rapidly than in the computational model cavity. Consequently, the recirculation zone in the physical model is shortened.

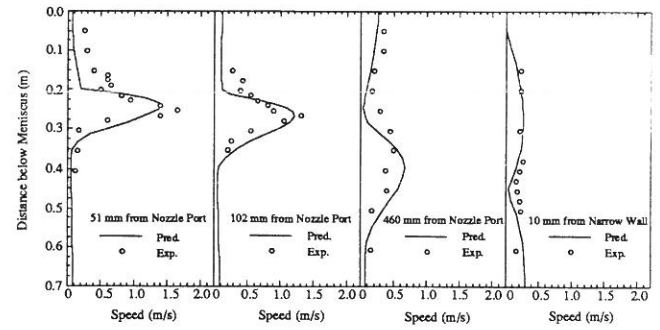
The flow predictions agree with the measurements that the effect of the gas bubbles on the flow pattern is quite small, for this particular case (with only 3% of gas injection). As seen in Table II, gas bubbles consistently raise the depth of the impingement point and the lower eye. Although small, the direction of movement of the upper eye does not agree. This might be due to the difficulty in measuring this location, which wanders with time and is not uniform through the thickness of the water model.

#### B. Comparison with Speed Measurements

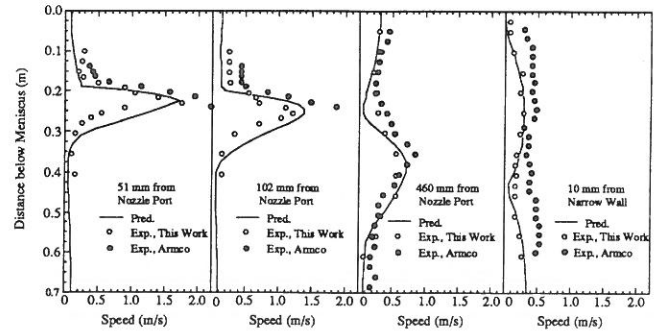
Predicted velocity profiles are compared in Figure 8 with experimental speed measurements on the Armco water model for simulation conditions corresponding to Cases A2 and A3 in Table I. This figure shows good agreement between predicted and measured velocities, both qualitatively and quantitatively. The results show how the jet evolves as it moves across the mold width. The jet spreads and its peak velocity decays, falling to about 30% of the inlet value by the time the jet is half way to the narrow face wall. Near the narrow face wall, the velocity profile has a concave shape which indicates the existence and location of the impingement point, where stagnation occurs. Note in Figure

**TABLE II. EXPERIMENTAL AND PREDICTED EYES AND IMPINGEMENT POINT IN WATER MODEL (CASE A1 IN TABLE I)**

	No Gas		With Gas	
	Pred.	Exp.	Pred. (Size 5 mm, 3% Gas)	Exp.
Lower Eye:				
Dist. to Centerline (m)	0.521	0.55	0.521	0.53
Depth (m)	1.143	0.80	1.041	0.76
Upper Eye:				
Dist. to Centerline (m)	0.521	0.55	0.579	0.53
Depth (m)	0.254	0.20	0.198	0.24
Impingement Point Depth (m)	0.498	0.50	0.442	0.48
Jet Angle (°)	25	28	25	29



(a). 51 mm (2 in.) by 89 mm (3.5 in.) rectangular nozzle port (Case A2 in Table I).



(b). Circular nozzle port with a diameter 51 mm (2 in.) (Case A3 in Table I).

**FIG. 8. Comparison of calculated and measured velocity profiles in water model (Case A2 and A3 in Table I).**

8(b) that speeds measured earlier (solid circles)<sup>[29]</sup> are larger than recent measurements (open circles), which agree more closely with the numerical predictions.

No major differences are seen between the velocities produced by the different nozzle port shapes compared in (a) and (b) of Figure 8. The characteristics of the rectangular and circular nozzle ports compared here are given in cases A2 and A3 in Table I. The separate 3-D model of nozzle flow found that these two nozzles produce jets with a similar angle, outlet area, and flow rate, despite differences in their nominal geometries.<sup>[16]</sup> Both the mathematical and physical models show that the two ports produce similar velocity profiles in the mold as well, except for a small difference in magnitude, which is reproduced by the calculations. This implies that the steady flow pattern in the mold is controlled solely by the angle, outlet area, and flow rate of the jet exiting the nozzle. Nozzle port shape alone should have no significant effect on the flow pattern and related phenomena. This might appear to contradict other work, which has reported an important influence of nozzle port shape on turbulence at the meniscus.<sup>[30]</sup> However, the present work concludes only that the nozzle port shape alone has no effect on the time-mean flow pattern. Nozzle shape might affect the casting process through its influence on non-steady phenomena, such as time-variations in turbulence or asymmetric surging, which require further study.

Figure 9 shows the similarity between the predicted and measured effects of gas bubble injection on the speed profiles down the mold interior. As observed visually, a 3% injection of 1 mm diameter helium bubbles has a relatively small effect on the jet. Predictions and measurements both show that gas injection widens the jet slightly and diminishes its peak. Quantitatively, the measurements are consistently



higher than the numerical predictions, as expected from the discussion of Figure 8(b).

Reasonable agreement between predicted and measured velocities is seen again in Figure 10, where the experimental data were obtained at Inland Steel<sup>[31]</sup> and correspond to the simulation conditions given in Case B1 of Table I. The velocity stagnation at the impingement point is particularly evident in this figure, which traverses speed very near to the narrow face wall (5mm). This stagnation point falls between adjacent high velocity peaks, where the jet splits to flow upward and downward along the narrow face. These measurements also show that the speed on the right side of the water model is higher than the left side, due to the asymmetrical opening of the nozzle slide gate.<sup>[31]</sup> This flow asymmetry was not accounted for in the numerical model results reported here. Nevertheless, the numerical model is able to reproduce the main flow characteristics, including the locations of impingement point and velocity peaks. Speed predictions match the measurements down the left wall quite closely. Note that relatively little difference is predicted between speeds at 7 mm and 14 mm from the wall.

It is interesting to note a slight overprediction of the measured velocity between 1 and 2m below the meniscus. This has been postulated to arise from the neglect of strand curvature in the numerical model, which was present in the physical model. As the strand curves away from the vertical nozzle, the greatest intensity jet down the narrow face wall should move closer to the outer radius. This should leave lower speeds at the center plane, where speeds are compared in Figure 10. This expected difference between predicted

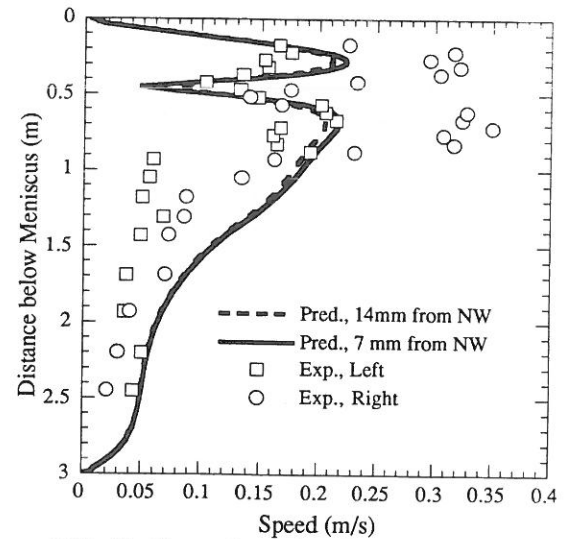


FIG. 10. Comparison of predicted and measured velocity profiles along narrow wall in water model (Case B1 in Table I).

and measured speeds due to this effect is surprisingly small, which indicates that flow tends to follow the strand curvature.

The greatest discrepancies between speed measurements and calculations exist in the low velocity areas of the mold. These include the velocity valley corresponding to the upper eye in the 460 mm frames of Figure 8, and the valley near the impingement point in the 10 mm frames of Figure 8 and Figure 10. Measured values in these regions are somewhat higher than the predictions for several reasons. This discrepancy is likely due to the well-known difficulty of measuring flow near separation, reattachment, or impingement points, which have low time-averaged velocity but high turbulence levels. The eyes and impingement points were observed to move around with time, so their locations are difficult to specify exactly. In addition, the single-sensor probe used in these experiments measures only speed (velocity magnitude) and cannot detect reversals of flow direction, such as caused by turbulence. Because speeds are always recorded as positive, larger time-averaged speeds are measured in these regions where rapid flow reversals are common. The same observation has been found for flow in nozzles.<sup>[16]</sup>

### C. Comparison with Gas Bubble Distribution Observations

Accurate calculation of bubble distribution is important because gas bubbles affect the liquid flow pattern in proportion to the calculated gas volume fraction,  $\sigma_g$ , in the present model. The calculated gas volume fractions and corresponding flow pattern are compared in Figure 11 with those observed at Inland Steel,<sup>[17, 31]</sup> under conditions B2 in Table I. The model predicts the same tendency for gas bubble movement as shown in the photograph. Most of the bubbles are crowded together in the upper region of the mold cavity. After entering the mold cavity with the liquid jet, the bubbles float quickly upward through the recirculation zone, and leave the top surface at their assumed terminal velocity,  $v_{gt}$  (0.24 m/s for 5 mm bubbles). Fewer and fewer bubbles stay in the jet as it travels across the mold.

This figure also shows that the flow pattern predictions are reasonable, and illustrates how the bubbles

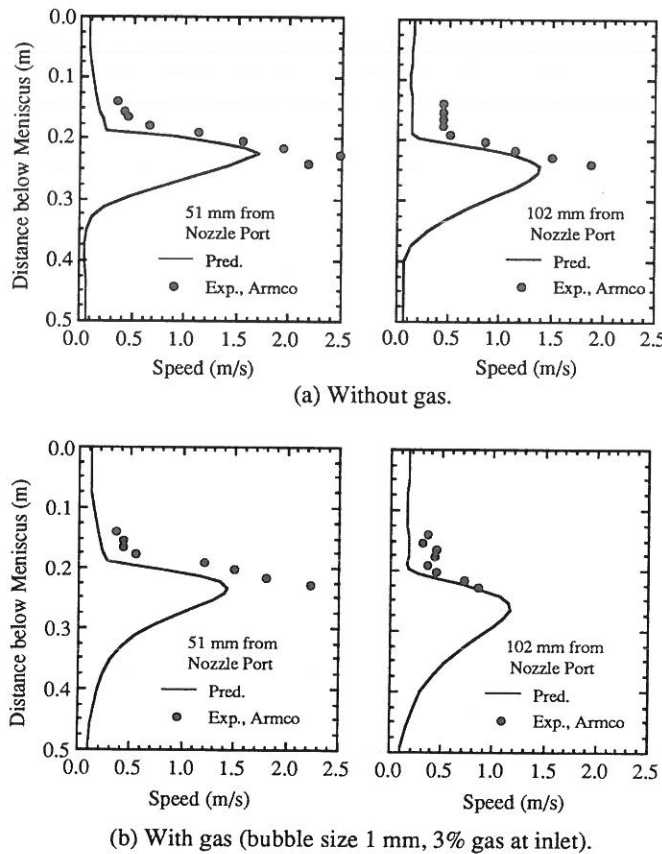


FIG. 9. Comparison of calculated and measured velocity profiles near nozzle port in water model (Case A2 in Table I).

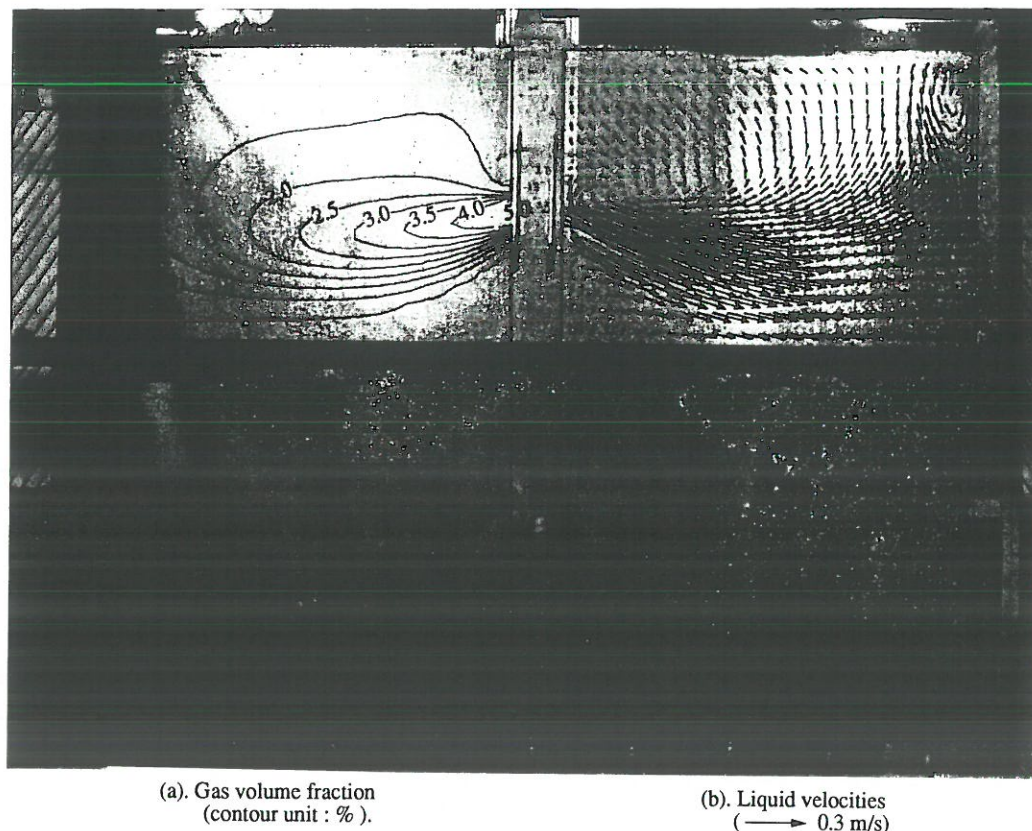


FIG. 11. Comparison of calculated and observed flow pattern and gas distribution in water model (Case B2 Table I).

buoy the liquid jet slightly upward. It is interesting to note that, for this particular narrow-mold geometry, a small, but significant recirculation region is predicted in the upper right corner at the narrow face meniscus. The extent of this phenomenon varies with gas injection rate and other casting conditions and is observed intermittently in the water model.

The model somewhat underpredicts bubble dispersion and penetration to the deeper portion of the mold cavity. Several reasons are suspected: (1) Stronger turbulence in the physical water model gives rise to higher turbulent dispersion than that predicted with the K- $\epsilon$  model; (2) Real, non-spherical bubbles have higher drag, so are carried further by the liquid jet. (3) Bubbles do not leave the top surface at their terminal velocity, as assumed by the model. Instead, they collect and coagulate under the action of surface tension forces, which likely prolongs their average residence time.

#### D. Verification of Heat and Mass Transfer Models

The heat and mass transfer models developed and described in this work have been verified using available data from plant trials, including measured liquid temperature,<sup>[23]</sup> shell thickness,<sup>[32]</sup> and slab composition.<sup>[28, 33]</sup> Further discussion of the details of these comparisons as well as model results and parametric studies is given elsewhere.<sup>[19, 26]</sup>

## VIII. EFFECT OF ARGON GAS INJECTION IN STEEL CASTER

The extensive validation with water models, presented in the last section, generates confidence that the numerical models are capable of making reasonable predictions of multi-phase-flow related phenomena, heat and mass transfer, in the mold region of actual continuous steel slab casters. The models are next applied to investigate the effects of argon gas injection on these phenomena under the typical casting conditions listed in Tables I (Case C) and III.

### A. Flow Pattern

Argon gas injection affects the casting process in part, through its influence on the liquid flow pattern. The extent of this effect depends on both the gas injection rate and the bubble size. Figures 12 and 13 show the effects of these two important parameters on the liquid flow patterns and the movement of gas bubbles themselves, for typical casting conditions, case C in Table I. The gas volume fraction and bubble size at the inlet (corresponding to the nozzle port), were calculated by considering the volume expansion that should occur as the bubbles heat up while traveling down the nozzle. This effect is expected to intensify the importance of argon gas in a steel caster, compared to that in a water model. The bubble expansion and the corresponding increase of gas volume flow rate into the mold are calculated according to Appendix I. The gas volume flow rate at the nozzle outlet will be raised generally by 3 to 5 times compared to that injected into the nozzle at ambient temperature and pressure. Setting the gas volume



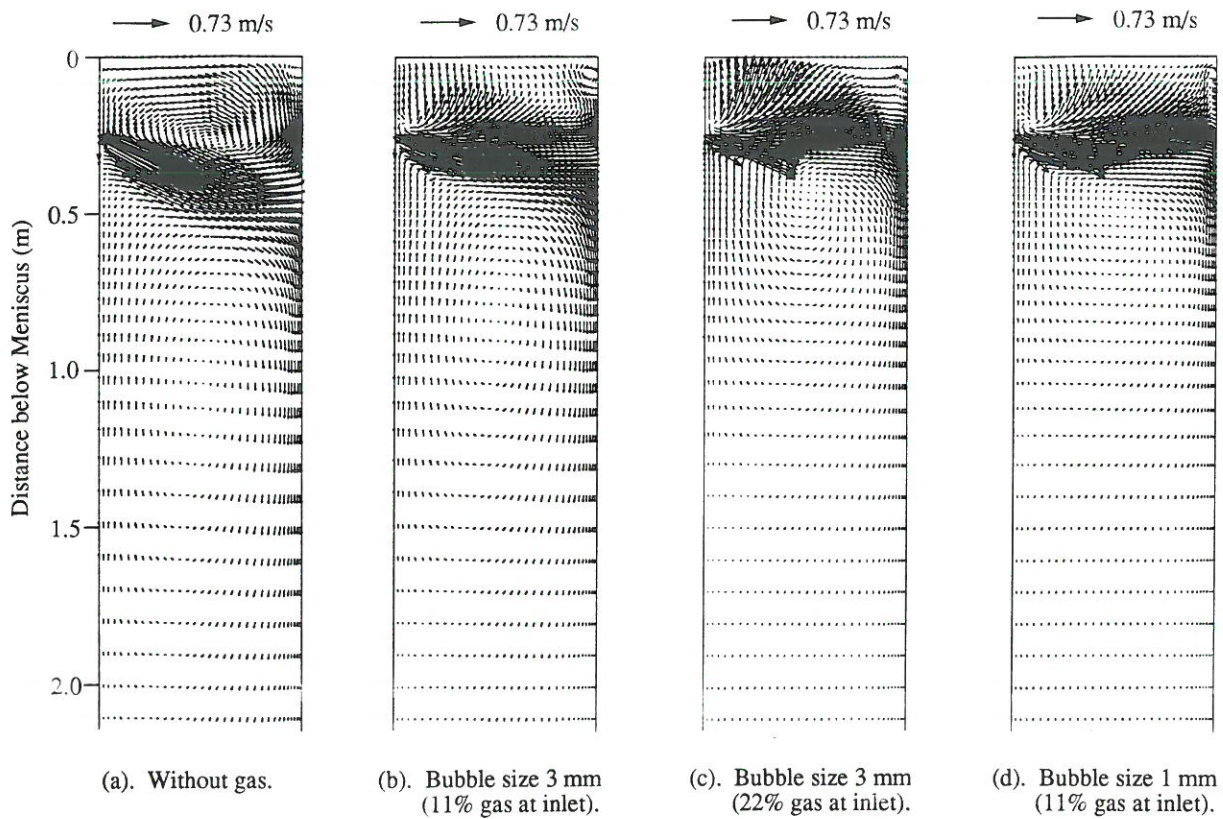


FIG. 12. Effect of argon gas bubble size and injection rate on flow pattern in steel caster.

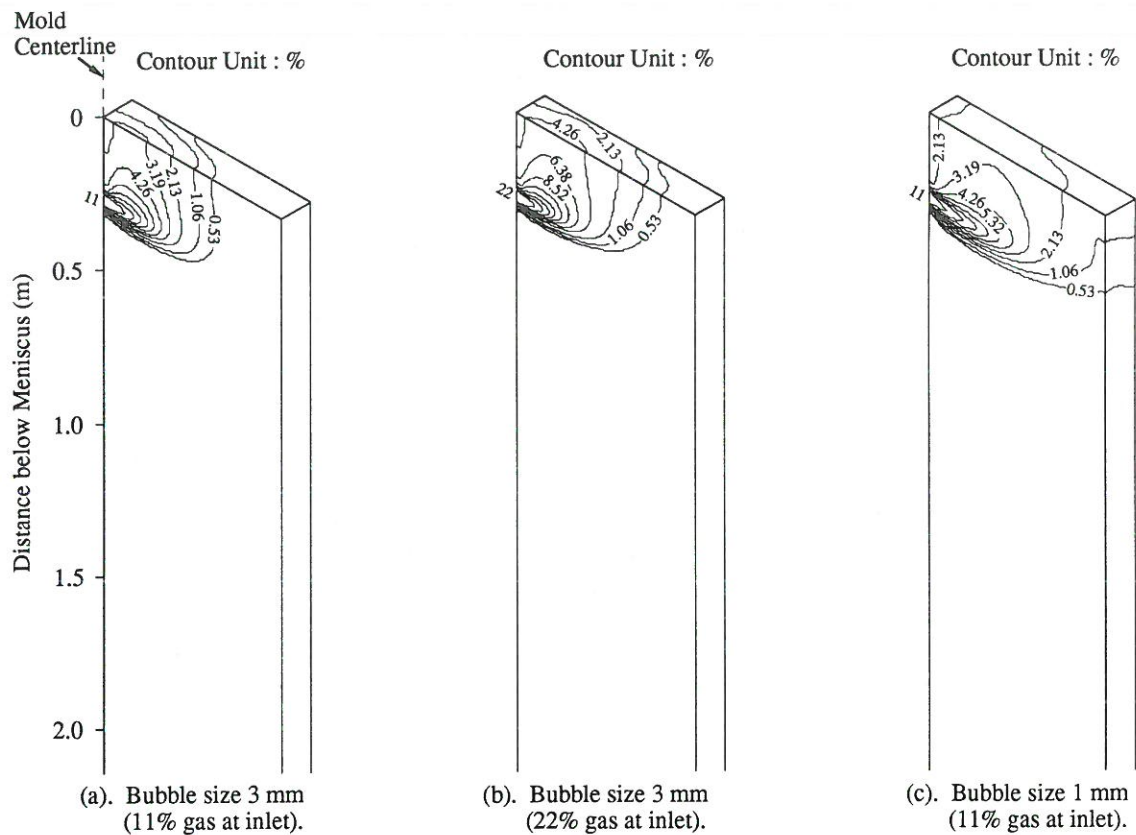


FIG. 13. Effect of argon gas bubble size and injection rate on distribution of gas volume fraction in steel caster.

TABLE III. SIMULATION CONDITIONS FOR  
HEAT TRANSFER MODEL<sup>†</sup>

$C_p$	680 J kg <sup>-1</sup> K <sup>-1</sup>
$h$	40 W m <sup>-2</sup> K <sup>-1</sup>
$k_o$	26 W m <sup>-1</sup> K <sup>-1</sup>
$Pr_o$	0.1
$Pr_t$	0.9
$T_{liq}$	1525 °C (2777 °F)
$T_o$	1550 °C (2822 °F)
$T_{sol}$	1518 °C
$T_\infty$	27 °C (81 °F)
$\Delta T_s$	25 °C (45 °F)

<sup>†</sup> Unlisted values are the same as Table I.

flow rate into the nozzle inlet at ambient temperature to be 0.00024 m<sup>3</sup>/s (30 SCFH or 5%), and expanding the initially 1 - 3 mm bubbles by five fold, produces a 22% volume fraction of 1.7 - 5 mm bubbles at the inlet to the mold. The argon flow rates of 0 - 22% with sizes of 1 - 5 mm were chosen in this study to represent the wide range of gas injection practices encountered in different casting operations.

#### 1. Effect of Gas Injection Rate

From figures 12 and 13, it is seen that increasing the gas volume flow rate entering the mold to 22% causes the upper recirculation zone to shrink to a very small region near the nozzle wall. The lower recirculation eye and impingement point shift upward remarkably. Stronger buoyancy due to introduction of more bubbles not only changes the flow pattern to larger extent, but also makes bubbles themselves float more easily, resulting in shallower bubble dispersion in the mold. The most important likely consequence of this change in flow pattern caused by large amounts of argon injection is a corresponding increase in surface turbulence, as bubbles break out and disturb flow at the top surface.

#### 2. Effect of Gas Bubble Size

Argon bubble size has an equally important effect. Larger bubbles are predicted to leave the mold faster and have less influence on the liquid flow pattern. A comparison of frames (b) and (d) in Figure 12, (a) and (c) in Figure 13 shows that smaller bubbles can penetrate further across the mold region. Deeply penetrating bubbles, particularly those few entering the lower recirculation zone, might be caught between dendrites of the solidifying shell and cause subsurface quality problems such as pinholes. Fortunately, the great volume expansion makes very small, easy-to-capture bubbles less likely to entrap.

The simulation predicts that more than 25% of the bubbles reach the upper portion of the wide face wall, during their upward flotation. This would imply that most trapped bubbles should be found in a shallow layer just under the surface of the central regions of the wide face. However, the high fluid velocities in this region make this unlikely for large bubbles. A much greater quality hazard is the surface turbulence generated when these large bubbles escape through the top surface.

#### B. Heat Transfer

The effect of argon injection on temperature and superheat dissipation is shown in Figures 14 to 18 and Table IV. Compared with the flat temperature distribution across most of the mold width when there is no gas, Figure 14(a), argon bubbles buoy hotter steel to the top surface and make liquid steel change its temperature from coldest (1527°C) at narrow face wall to highest (1531°C) half way across the mold, then to medium (1529°C) close to the nozzle wall (Figure 14(b)). This matches the temperature distribution measured in a steel caster by Offerman.<sup>[23]</sup>

Figures 15 through 18 and Table IV show effect of argon injection on the "superheat flux" transported across the interface between the liquid steel and the solidifying shell against the narrow and wide faces. The peak superheat flux associated with the narrow face impingement point is slightly lower (575 kW/m<sup>2</sup>) than that without gas (625 kW/m<sup>2</sup>). Argon gas also produces a substantial increase in superheat flux to the upper regions of the wide face, and the meniscus region in particular. The bubbles shift the hotter region upward in the mold so that a greater portion of the superheat is removed in the casting mold (0.6 m from meniscus) and hottest impingement point moves further above the mold exit. These side-effects of argon use could be beneficial in decreasing the potential dangers of shell thinning along the narrow face and meniscus freezing. However, these small effects are probably of secondary importance to the effects of argon on flow pattern, surface turbulence and inclusion motion.

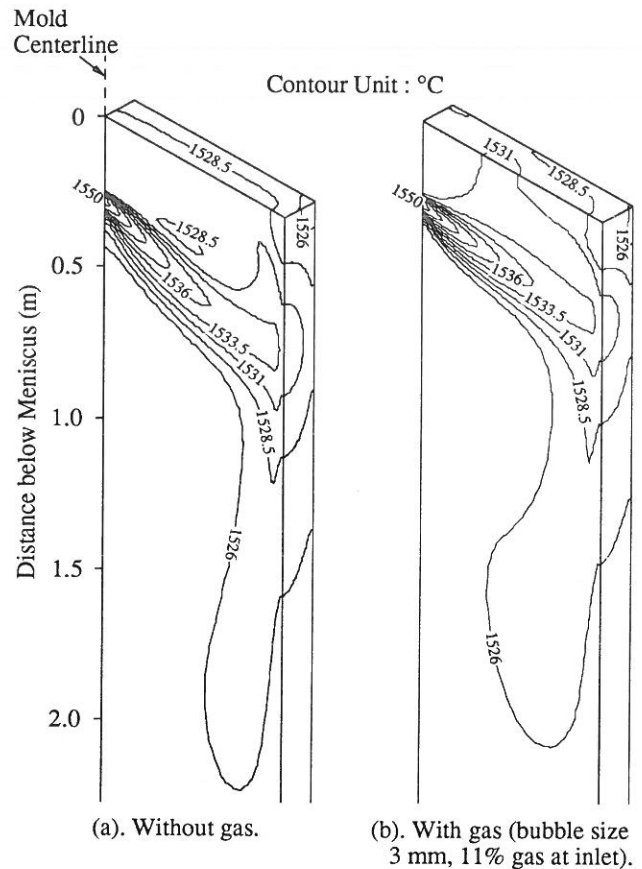


FIG. 14. Effect of argon gas bubbles on temperature distribution in steel caster.



### 1. Effect of Gas Injection Rate

Increasing argon injection rate amplifies its effect on heat transfer, similar to its effect on the flow pattern. This is shown in Figure 17 and Table IV. Increasing injection

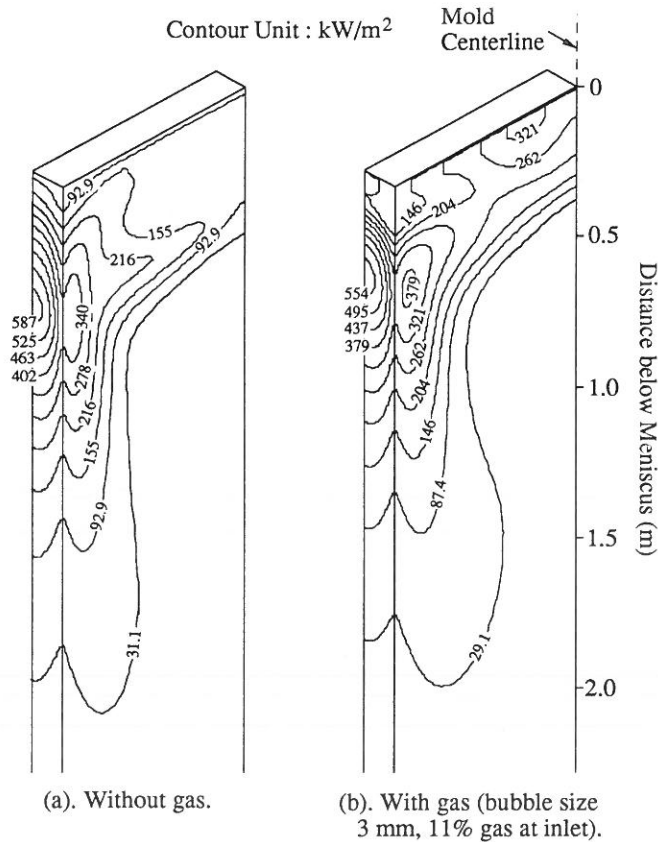


FIG. 15. Effect of argon gas bubbles on heat flux distribution in steel caster.

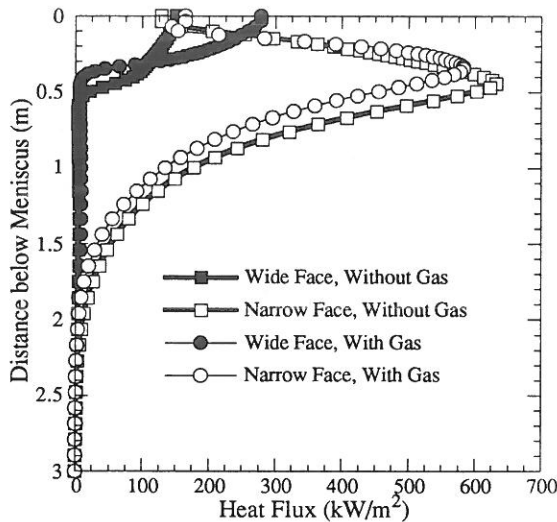


FIG. 16. Effect of argon gas bubbles on heat flux along centerlines of wide and narrow faces (bubble size 3 mm, 11% gas at inlet).

causes a further upward-shift of impingement point and a bigger drop of the heat flux peak value. It should be noticed that more than 80% of the total superheat is transferred to the wide face for the case with 22% of 3 mm bubbles (Table IV). This compares to 70% for the case without gas.

### 2. Effect of Gas Bubble Size

The effect of gas bubble size can be seen in Figure 18 and Table IV. The smaller the bubbles, the stronger their effect. The narrow face impingement point shifts upward and the peak value of heat flux decreases systematically with decrease of bubble size (Figure 18). The total superheat transferred to the shell inside the casting mold increases from 60% (without gas or with 5 mm bubbles), to 65% (with 3 mm bubbles) to 74% (with 1 mm bubbles). Heat delivered to the meniscus increases in a similar manner. These findings imply a potential benefit from smaller bubbles. On the other hand, because they penetrate further into the strand, smaller bubbles are more easily trapped by the solidifying

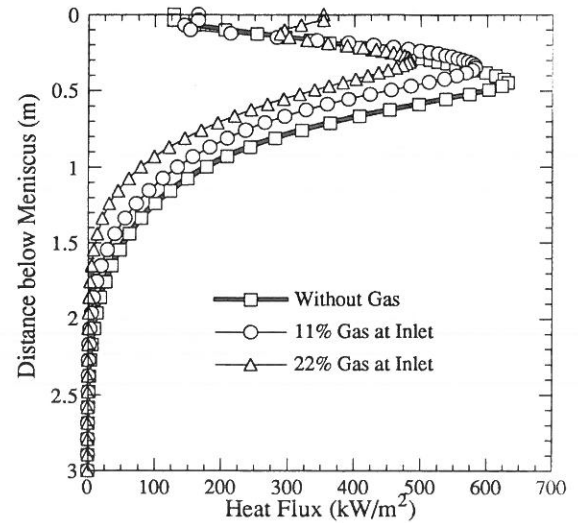


FIG. 17. Effect of argon gas injection rate on heat flux along narrow face centerline (bubble size 3 mm).

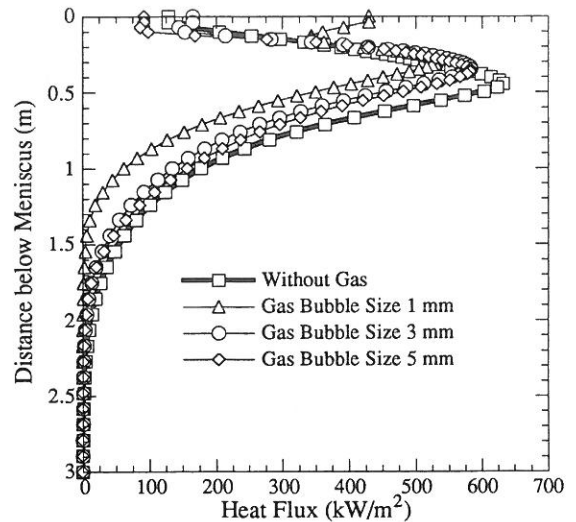


FIG. 18. Effect of argon gas bubble size on heat flux along narrow face centerline (11% gas at inlet).

TABLE IV. PREDICTED SUPERHEAT DISTRIBUTION

Superheat lost to:	Without Gas		Size 5 mm, 11% Gas		Size 3 mm, 11% Gas		Size 1 mm, 11% Gas		Size 3 mm, 22% Gas	
	Heat flow (kW)	pct	Heat flow (kW)	pct	Heat flow (kW)	pct	Heat flow (kW)	pct	Heat flow (kW)	pct
Conduction through top surface flux layer	11.3	1.9	11.3	1.9	11.3	1.9	11.3	1.9	11.3	1.9
Convection to shell inside mold (0 - 0.6m)										
Narrow face	99.7	17.1	92.3	15.9	91.6	15.7	91.6	15.7	82.1	14.1
Wide face	255.1	43.8	256.2	44.0	290.3	49.9	340.7	58.5	307.6	52.9
Convection to shell just below mold (0.6 - 1.6m)										
Narrow face	67.5	11.6	56.0	9.6	49.2	8.5	25.6	4.4	30.7	5.3
Wide face	118.2	20.3	147.3	25.3	123.2	21.2	117.7	20.2	150.5	25.9
Convection to shell farther below mold (1.6 - 3.0m)										
Narrow face	4.8	0.8	2.2	0.4	2.4	0.4	0.3	0.1	0.7	0.1
Wide face	37.3	6.4	31.2	5.4	28.3	4.9	7.3	1.3	12.1	2.1
Dissipation very low in caster (below 3.0m)	0.9	0.2	0.5	0.1	0.5	0.1	0.0	0.0	0.1	0.0
Total	594.8	102.2	597.0	102.6	596.8	102.5	594.5	102.1	595.1	102.3
Superheat into mold	582.0		582.0		582.0		582.0		582.0	
Numerical errors	12.8	2.2	15.0	2.6	14.8	2.5	12.5	2.1	13.1	2.3

shell, which increases the danger of pinholes. It is suspected that an optimum range of bubble size exists between 1 and 5 mm in diameter.

### C. Mass Transfer

The effect of argon gas bubbles on slab composition during a steel grade transition was investigated by running the 3-D mass transfer model, described in Section IV, under the conditions listed as Case C in Table I (both without gas and with 11% of 3 mm bubbles). A solidification constant,  $k_{shell}$ , of  $0.00327 \text{ ms}^{-0.5}$  was assumed for the parabolic shell growth function, which generates a liquid pool length (metallurgical length) of 19.6 m.

The resulting composition profiles down the solid slabs are shown in Figure 19. Surface composition changes slightly when argon is introduced into the casting mold. Argon injection transports new grade to the meniscus faster, thereby slightly reducing the extent of intermixing along the slab surface.

There is no measurable change in mixing along the centerline of the slab, however. The effect of argon gas on slab composition is smaller than that on superheat removal because bubbles only affect very small region of the upper portion of the strand (less than 0.5 m). The slab composition depends on mass transfer in the entire liquid pool, which is more than an order of magnitude longer. The effect of argon decays very rapidly with distance from the meniscus, and almost completely disappears below about 3m

down the strand, where the solidified shell is only about 45 mm thick. Thus, internal mixing behavior below this depth is expected to be unchanged, as observed in Figure 19. Intermixing of grades extends to a significant distance down the slab centerline and is governed by turbulent diffusion, as discussed and verified in previous work.<sup>[26]</sup>

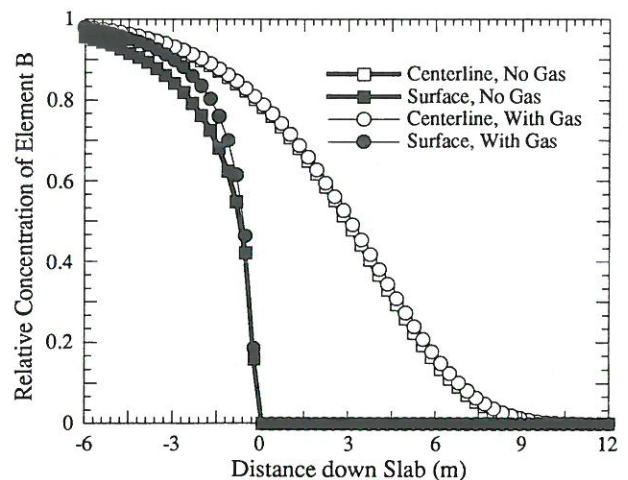


FIG. 19. Effect of argon bubbles on composition along slab centerline during a steel grade transition (bubble size 3 mm, 11% gas at inlet).



## IX. CONCLUSIONS

1. Mathematical models have been developed to predict multiphase flow in the continuous slab casting process and its associated heat and mass transfer. The models are being applied to understand complex flow related phenomena in the process.
2. Good agreement has been obtained between the flow model predictions and observations of flow pattern characteristics and speed measurements. Thus, the standard K- $\epsilon$  turbulence model appears able to reasonably reproduce steady state flow in a continuous casting mold, even when there is gas injection. Other parts of the model have been validated through comparison with other experimental data.
3. Both experimental and predicted results show that there is little difference between the time averaged flow patterns from rectangular and round nozzle ports, with similar jet outlet area, jet angle, and casting conditions.
4. Argon gas bubble injection changes the liquid flow pattern most in the upper portion of the mold. The impingement point and recirculation centers shift upward while the lower portion of the mold is affected much less.
5. The effects of argon gas in a steel caster are expected to be intensified, relative to the water model, due to gas volume expansion at high temperature and the corresponding increase of flow rate into the mold.
6. Increasing gas injection rate or decreasing bubble size both intensify the changes in the flow pattern.
7. Larger bubbles float more easily and leave the mold faster, so have less effect on the flow pattern, but possibly more effect on surface turbulence.
8. Smaller bubbles penetrate deeper into the liquid pool, increasing their likelihood of entrapment into the solidifying shell, causing pinholes.
9. Argon gas injection causes superheat to be removed higher in the caster, moves the hot spot upwards, lowers the peak heat flux, and delivers more heat to the wide face and meniscus regions.
10. During a steel grade transition, argon injection only slightly affects slab surface composition, and has no effect on intermixing in the slab interior.

## ACKNOWLEDGMENTS

The authors wish to thank R. Sussman, T. Tucker, and J. Hester of Armco Inc., (Middletown, OH) and Y.H. Wang of Inland Steel Corp. (East Chicago, IN) for their assistance obtaining measurements on their company water models and providing data. The steel companies: Armco Inc., Inland Steel Corp., LTV Steel (Cleveland, OH) and BHP Co. Ltd. (Wallsend, Australia) and the National Science Foundation (Grant No. MSS-8957195) are gratefully acknowledged for funding which made this research possible. Finally, thanks are due to Fluid Dynamics Inc., (Evanston, IL) for use of FIPOST and to the National Center for Supercomputing Applications at the University of Illinois for time on the Cray supercomputers.

## APPENDIX I. GAS EXPANSION IN CASTERS

The gas state equation:

$$\rho_g = \frac{P_g}{R T_g} \quad [A1.1]$$

where  $P_g$  is pressure inside the gas bubbles,  $\rho_g$  is gas material density,  $T_g$  is gas bubble temperature,  $R$  is universal gas constant.

The mass of a gas bubble can be expressed as:

$$m_g = \frac{\pi}{6} d_g^3 \rho_g \quad [A1.2]$$

where  $d_g$  is the hydraulic diameter of the gas bubble.

When the bubble moves from nozzle gate to outlet port, the relations of pressure, density, temperature, and size of the same gas bubble can be obtained:

$$\frac{\rho_{gp}}{\rho_{gi}} = \frac{P_{gp}}{P_{gi}} \frac{T_{gi}}{T_{gp}} \quad [A1.3]$$

$$\frac{d_{gp}}{d_{gi}} = \left( \frac{\rho_{gi}}{\rho_{gp}} \right)^{\frac{1}{3}} \quad [A1.4]$$

where the subscripts "i" and "p" denote "nozzle inlet", which corresponds to the nozzle gate, and "nozzle outlet port" respectively.

Assumptions:

1. Argon gas is injected near the gate of the submerged entry nozzle (bottom of the tundish) at room temperature and pressure, i.e.:

$$\rho_{gi} = 1.61 \text{ kg/m}^3$$

$$P_{gi} = P_{\infty} = 100500 \text{ N/m}^2$$

$$T_{gi} = T_{\infty} = 298 \text{ K}$$

2. The pressure at the meniscus is 1 atm and the submerged depth of the SEN is 0.3 m, so that the pressure at the outlet port of the SEN is calculated as:

$$P_{gp} = P_{\infty} + \rho_g L_n = 100500 + 7020 \cdot 9.8 \cdot 0.3 = 121139 \text{ N/m}^2$$

3. Gas bubbles are heated by liquid steel so fast that their temperature reaches 1500 °C when they arrive at the SEN outlet port, i.e.:

$$T_{gp} = 1773 \text{ K}$$

Then we can get the gas density, average hydraulic diameter of gas bubbles, and the bubble volume expansion at the SEN outlet port:

$$\begin{aligned} \rho_{gp} &= \rho_{gi} \frac{P_{gp}}{P_{gi}} \frac{T_{gi}}{T_{gp}} = 1.6 \frac{121139}{100500} \frac{298}{1773} \\ &= 0.3241 \text{ kg/m}^3 \end{aligned}$$

$$d_{gp} = d_{gi} \left( \frac{\rho_{gi}}{\rho_{gp}} \right)^{\frac{1}{3}} = d_{gi} \left( \frac{1.6}{0.3241} \right)^{\frac{1}{3}} = 1.7 d_{gi}$$

$$\text{gas volume expansion} = \frac{\rho_{gi}}{\rho_{gp}} = \frac{1.6}{0.3241} = 4.9$$

Gas bubble volume expands almost 5 times and the effective bubble diameter increases 1.7 times.

## APPENDIX II. GAS VOLUME FRACTION AT THE NOZZLE PORT

According to the definition of gas volume fraction, we have:

$$\sigma_{g0} = \frac{(\text{gas volume flow rate})_{\text{nozzle port}}}{(\text{total volume flow rate})_{\text{nozzle port}}} \quad [\text{A2.1}]$$

According to the calculation in Appendix I and mass balance of gas phase in the nozzle and in the mold, assuming gas is injected right at the nozzle inlet at room temperature and pressure, the gas volume fraction at the inlet of the mold cavity can be obtained:

$$\sigma_{g0} = \frac{Q_g \left( \frac{1}{V_c N W} \frac{1}{1 - \sigma_{out}} \frac{T_0}{T_{\infty}} \frac{p_{\infty}}{p_{\infty} + \rho g L_n} \right)}{1 + Q_g \left( \frac{1}{V_c N W} \frac{1}{1 - \sigma_{out}} \frac{T_0}{T_{\infty}} \frac{p_{\infty}}{p_{\infty} + \rho g L_n} \right)} \quad [\text{A2.2}]$$

where  $\sigma_{out}$  = gas volume fraction at outlet of the domain

$$p_{\infty} = \text{room pressure} = 100500 \text{ N/m}^2$$

$$T_{\infty} = \text{room temperature (K)}$$

$$Q_g = \text{gas injection rate at the nozzle inlet (m}^3/\text{s)}$$

and other variables are listed in Nomenclature.

Generally,  $\sigma_{out}$  is negligibly small, so Equation [A2.4] is simplified to:

$$\sigma_{g0} = \frac{Q_g \left( \frac{1}{V_c N W} \frac{T_0}{T_{\infty}} \frac{p_{\infty}}{p_{\infty} + \rho g L_n} \right)}{1 + Q_g \left( \frac{1}{V_c N W} \frac{T_0}{T_{\infty}} \frac{p_{\infty}}{p_{\infty} + \rho g L_n} \right)} \quad [\text{A2.3}]$$

## NOMENCLATURE

C	relative concentration in strand
$C_p$	specific heat (liquid steel) ( $\text{J kg}^{-1} \text{K}^{-1}$ )
$d_g$	hydraulic diameter of gas bubbles (mm)
E	wall roughness constant (in K-ε wall laws)
F	mass fraction of a given element
h	Heat transfer coefficient (top surface) ( $\text{W m}^{-2} \text{K}^{-1}$ )
$K_o$	turbulent kinetic energy (at inlet) ( $\text{m}^2 \text{s}^{-2}$ )
$k_o$	laminar thermal conductivity ( $\text{W m}^{-1} \text{K}^{-1}$ )
$k_{shell}$	solidification constant ( $\text{m s}^{-0.5}$ )
$L_o$	nominal nozzle submergence depth (from top surface to top of nozzle port) (m)
$L_h$	inlet height (mm)
$L_w$	inlet width (mm)
$L_n$	jet submergence depth (from top surface to top of the jet) (m)
N	strand thickness (across narrow face) (m)
n	normal direction of boundaries
p	static pressure (relative to outlet plane of domain) ( $\text{N s}^{-2}$ )
$Pr_o$	laminar Prandtl Number, ( $C_p \mu_o k_o^{-1}$ )
$Pr_t$	turbulent Prandtl Number
$Q_g$	gas injection rate (entering nozzle gate) ( $\text{m}^3 \text{s}^{-1}$ )
Re	Reynolds number ( $V_c \sqrt{N W} \rho \mu^{-1}$ )
$q_{sh}$	superheat flux from liquid steel to solidifying shell ( $\text{W m}^{-2}$ )
$Sc_t$	turbulent Schmidt number
T	temperature ( $^{\circ}\text{C}$ )
$T_o$	casting temperature (pour temperature) (at inlet) ( $^{\circ}\text{C}$ )
$T_{liq}$	liquidus temperature ( $^{\circ}\text{C}$ )
$T_{sol}$	solidus temperature ( $^{\circ}\text{C}$ )
$T_{\infty}$	ambient temperature ( $^{\circ}\text{C}$ )
$V_c$	casting speed ( $\text{m s}^{-1}$ )
$v_{gt}$	gas bubble terminal velocity ( $\text{m s}^{-1}$ )
$v_{xo}$	normal velocity through inlet (peak) ( $\text{m s}^{-1}$ )
$v_{zo}$	downward velocity through inlet ( $\text{m s}^{-1}$ )
W	strand width (across wide face) (m)
Z	strand length simulated (m)
z	distance down strand or slab (m)
$\alpha$	jet angle (at inlet) ( $^{\circ}$ )
$\alpha_o$	nominal angle of nozzle port edges (at inlet) ( $^{\circ}$ )
$\Delta T_s$	superheat temperature ( $T_o - T_{liq}$ ) ( $^{\circ}\text{C}$ )
$\epsilon_o$	dissipation rate (at inlet) ( $\text{m}^2 \text{s}^{-3}$ )
$\mu_o$	laminar (molecular) viscosity ( $\text{kg m}^{-1} \text{s}^{-1}$ )
$\rho$	density (liquid) ( $\text{kg m}^{-3}$ )
$\sigma_g$	gas volume fraction (%)
$\sigma_{g0}$	gas volume fraction (at inlet) (%)

## REFERENCES

1. M. Salcudean and K.Y.M. Lai: "Computation of Three-Dimensional Flow Associated with Heat and Mass Transfer in Gas-Agitated-Liquid Reactors", *Numerical Heat Transfer*, 1988, vol. 14, pp. 97-111.
2. M. Salcudean, K.Y.M. Lai and R.I.L. Guthrie: "Multi-Dimensional Heat, Mass and Flow Phenomena in Gas-Stirred Reactors", *Can. J. Chem. Eng.*, 1984, vol. 63, pp. 51-61.



3. M. Salcudean, C.H. Low, A. Hurda and R.I.L. Guthrie: "Computation of Three-Dimensional Flow and Heat Transfer in Gas-Agitated Reactors", *Chem. Eng. Commun.*, 1983, vol. 21, pp. 89-103.
4. D. Mazumdar and R.I.L. Guthrie: "Hydrodynamic Modeling of Some Gas Injection Processes in Ladle Metallurgy Operations", *Metal. Trans.*, 1985, vol. 16B, pp. 83-90.
5. T.D. Roy, A.K. Majumdar and D.B. Spalding: "Predicting Fluid Flow in Gas-Stirred Systems", *J. Met.*, 1981, (November), pp. 42-47.
6. J. Szekely, N. El-Kaddah and J.H. Grevet: "Flow Phenomena in Argon-Stirred Ladles, Room Temperature Measurements and Analysis", *Int. Conf. Injection Metallurgy*, 1980, pp. 5:1-5:32.
7. J. Szekely, H.Y. Wang and K.M. Kiser: "Flow Pattern, Velocity and Turbulent Energy Measurements and Predictions in a Water Model of an Argon-Stirred Ladle", *Metall. Trans.*, 1976, vol. 7B, pp. 287-295.
8. P.E. Anagbo and J.K. Brimacombe: "Plume Characteristics and Liquid Circulation in Gas Injection through a Porous Plug", *Metall. Trans.*, 1990, vol. 21B, pp. 637-648.
9. A.H. Castillejos and J.K. Brimacombe: "Measurements of Physical Characteristics of Bubbles in Gas-Liquid Plumes: Part I. An Improved Electroresistivity Probe Technique", *Metall. Trans.*, 1987, vol. 18B, pp. 649-658.
10. A.H. Castillejos and J.K. Brimacombe: "Measurements of Physical Characteristics of Bubbles in Gas-Liquid Plumes: Part II. Local Properties of Turbulent Air-Water Plumes in Vertically Injected Jets", *Metall. Trans.*, 1987, vol. 18B, pp. 659-671.
11. Y.Y. Sheng and G.A. Irons: "Turbulence Modeling of Plume Flows in a Gas Stirred Ladle", *Process Technology Conference (75th Steelmaking Conference)*, The Iron and Steel Society, Warrendale, PA, 1992.
12. S.T. Johansen and F. Boysan: "Fluid Dynamics in Bubble Stirred Ladles: Part II. Mathematical Modeling", *Metall. Trans.*, 1988, vol. 19B, pp. 755-764.
13. S.T. Johansen, D.G.C. Robertson, K. Woje and T.A. Engh: "Fluid Dynamics in Bubble Stirred Ladles: Part I. Experiments", *Metall. Trans.*, 1988, vol. 19B, pp. 745-754.
14. N. Bessho, R. Yoda and H. Yamasaki: "Numerical Analysis of Fluid Flow in Continuous Casting Mold by Bubble Dispersion Model", *Iron and Steelmaker*, 1991, vol. 18 (4), pp. 39-44.
15. S.L. Soo: *Fluid Dynamics of Multiphase System: Chapter 3 Transport Processes of a Deformable Particle*, Blaisdell Publishing Co., Waltham, MA, 1967.
16. D.E. Hershey, B.G. Thomas and F.M. Najjar: "Turbulent Flow through Bifurcated Nozzles", to appear in *Int. J. for Numerical Methods in Fluids*, 1993.
17. B.G. Thomas, L.M. Mika and F.M. Najjar: "Simulation of Fluid Flow and Heat Transfer Inside a Continuous Slab Casting Machine", *Metall. Trans.*, 1990, vol. 21B, pp. 387-400.
18. F.M. Najjar: *Finite-Element Modeling of Turbulent Fluid Flow and Heat Transfer through Bifurcated Nozzles in Continuous Steel Slab Casters*, M.S. Thesis, University of Illinois at Urbana-Champaign, 1990.
19. X. Huang, B.G. Thomas and F.M. Najjar: "Modeling Superheat Removal during Continuous Casting of Steel Slabs", *Metall. Trans.*, 1992, vol. 23B, pp. 339-356.
20. X. Huang: *Studies on Turbulent Gas-Particle Jets and 3-D Turbulent Recirculating Gas-Particle Flows*, Ph.D. Thesis, Tsinghua University, Beijing, P. R. China, 1988.
21. S.V. Patankar: *Numerical Heat Transfer and Fluid Flow*, McGraw-Hill, New York, NY, 1980.
22. B.E. Launder and D.B. Spalding: "The Numerical Computation of Turbulent Flows", *Computer Methods Appl. Mech. Eng.*, 1974, vol. 3, pp. 269-289.
23. C. Offerman: "Internal Structure in Continuously Cast Slabs by the Metal Flow in the Mould", *Scand. J. Metall.*, 1981, vol. 10, pp. 25-28.
24. P. Flint: "A Three-dimensional Finite Difference Model of Heat Transfer Fluid Flow and Solidification in the Continuous Slab Caster", *Proceedings of 73rd Steel Making Conference*, ISS/AIME, Warrendale, PA, 1990, Vol. 73, pp. 481-490.
25. B.G. Thomas, W.R. Storkman and A. Moitra: "Optimizing Taper in Continuous Slab Casting Molds Using Mathematical Models", *The Sixth International Iron and Steel Congress*, ISIJ, Tokyo, Japan, 1990, Vol. 2, pp. 348-355.
26. X. Huang and B.G. Thomas: "Modeling of Steel Grade Transition in Continuous Slab Casting Processes", to appear in *Metall. Trans.*, April issue of 1993.
27. M.S. Engelman: *FIDAP Theoretical Manual -- Revision 4.0*, Fluid Dynamics International, Inc., Evanston, IL, 1986.
28. R. Sussman and J. Schade: Armco Inc., private communication, 1992.
29. R. Sussman, T. Tucker and J. Hester: Armco Inc., unpublished research, 1992.
30. J. Birat, M. Larrecq, J. Lamant and J. Petegnief: "The Continuous Casting Mold: A Basic Tool for Surface Quality and Strand Productivity", in *Mold Operation for Quality and Productivity*, Iron and Steel Society, Warrendale, PA, 1991, pp. 3-14.
31. Y.H. Wang: "3-D Mathematical Model Simulation on the Tundish Slide Gate and Its Effect in the Continuous Casting Mold", *Process Technology Conference (75th Steelmaking Conference)*, L.G. Kuhn, eds., The Iron and Steel Society, Warrendale, PA, 1992, Vol. 10.
32. M. Kumada and I. Mabuchi: *Trans. Japan. Soc. Mech. Eng.*, 1969, vol. 35, pp. 1053-1061.
33. R. Gas: Inland Steel, Inc., private communication, 1992.